Enhanced Repetitive Control with Phase Compensation based ADRC for Harmonic Suppression in Magnetically Suspended Rotor under Strong Gyroscopic Effects

Yuxiang Zhu, Fanqiang Gao, *Member*, *IEEE*, Kaiyu Shan, Zixin Li, *Senior Member*, *IEEE*, and Yaohua Li, *Member*, *IEEE*

***Abstract*—Magnetically suspended rotor (MSR) systems have gained widespread industrial adoption owing to their frictionless operation and exceptional reliability. However, harmonic current generated by unbalanced mass and sensor runout threatens the system stability. Repetitive control (RC) effectively suppresses harmonic current, but its parameter design relies on an accurate decoupling model of the system. The decoupling model for the MSR system is often simplified to a second-order linear system. Such a simplification, however, necessitates explicit consideration of system uncertainties caused by unmodeled nonlinearities during the RC design process. Especially under strong gyroscopic effects, the parameter uncertainty is further increased. In this article, an active disturbance rejection controller (ADRC) based on phase compensation (PC) is used to suppress coupling disturbances and improve the control performance of harmonic suppression. Firstly, the dynamic model of the MSR system is established, and both internal and external disturbances are thoroughly analyzed. Then, the RC-PCADRC scheme is designed, integrating the complementary strengths of RC and ADRC, with a particular emphasis on PC to improve stability margins. A comprehensive stability analysis is conducted, along with parameter optimization guidelines. Finally, the effectiveness and superiority of the proposed scheme are validated through both simulations and experiments.**

***Index Terms*—Magnetically suspended rotor (MSR), Harmonic current, Gyroscopic effects, Repetitive control (RC), Active disturbance rejection controller (ADRC).**

Manuscript received October 23, 2025; revised December 18, 2025; accepted January 13, 2026. Date of publication March 25, 2026; Date of current version March 20, 2026.

This work was supported by the Youth Innovation Promotion Association CAS under Grant 2023042 and the Major Science Facility Project of the Shandong Provincial Natural Science Foundation under Grant ZR2022DKX005.

Yuxiang Zhu and Kaiyu Shan are with the State Key Laboratory of High Density Electromagnetic Power and Systems, Institute of Electrical Engineering, Chinese Academy of Sciences, Beijing 100190, China and also with the University of Chinese Academy of Sciences, Beijing 100049, China (e-mail: zhu-yx23@mail.iee.ac.cn; shankaiyu@mail.iee.ac.cn).

Fanqiang Gao, Zixin Li, and Yaohua Li are with the State Key Laboratory of High Density Electromagnetic Power and Systems, Institute of Electrical Engineering, Chinese Academy of Sciences, Beijing 100190, China and also with the University of Chinese Academy of Sciences, Beijing 100049, China, and also with the Shandong Provincial Key Laboratory of Advanced Electromagnetic Conversion Technology, Qilu Zhongke Institute of Electrotechnical Advanced Electromagnetic Drive Technology, Jinan 250104, China (e-mail: gaofanqiang@mail.iee.ac.cn; lzx@mail.iee.ac.cn; yhli@mail.iee.ac.cn).

(*Corresponding authors: Fanqiang Gao*)

Digital Object Identifier 10.30941/CESTEMS.2026.00003

I. INTRODUCTION

MAGNETIC suspension technology has been widely used in bearing applications due to its characteristics, including frictionless operation, lubrication-free design, high rotational speeds, and active controllability, which have attracted increasing research attention [1]-[2]. Compared with conventional mechanical bearings, magnetically suspended rotor (MSR) system demonstrates superior performance in vibration suppression and system stability through closed-loop electromagnetic force control, with successful applications in turbomachinery, flywheel energy storage, and other high-precision industrial systems [3]-[6]. The MSR system typically employs hybrid magnetic levitation, utilizing both active magnetic bearing (AMB) and passive magnetic bearing (PMB) components for rotor suspension. However, AMB requires current excitation during operation, and current harmonics degrade rotor stability. Harmonic current in AMB arises primarily from rotor mass imbalance and sensor runout [7]. Mass eccentricity induces synchronous current, while sensor misalignment and nonuniform electromagnetic properties generate integer-order harmonic current [8]. The current harmonics acting on MSR induce additional rotor vibration, leading to increased power consumption, casing vibration, acoustic noise generation, and reduced system reliability [9].

Several harmonic suppression techniques have been developed for MSR systems, including least mean square [10], resonance controllers [11], and notch filters [12]. Notably, the repetitive control (RC) stands out by employing the internal model principle to effectively eliminate periodic disturbances with known frequencies but unknown amplitudes [13]. Due to its effectiveness, RC has been widely adopted in power systems and power electronics for harmonic suppression [14]-[15]. However, the MSR system's open-loop instability and positive displacement stiffness make it sensitive to controller parameters, presenting a significant

challenge for stabilizing the system under RC control. Previous studies have demonstrated that incorporating phase compensation (PC) into RC can preserve system stability [16]. Concurrently, structural modifications to conventional RC architectures have been shown to improve harmonic suppression capabilities in MSR systems [17]-[19]. However, these RC-based approaches are implemented based on a single-degree-of-freedom decoupling model of the magnetic bearing system. For slender rotors, MSR systems can be approximated as five single-degree systems due to negligible gyroscopic effects, enabling decentralized control. However, flat rotors exhibit significant gyroscopic coupling in radial directions, inducing radial coupling dynamics [20]. This challenge is particularly critical for hydro turbines employing MSR, as their guide bearings typically feature substantial width and mass [21]. Hence, in the design of MSR system for a hydro turbine, gyroscopic effects must be considered as a critical factor.

Recently, several control approaches have been proposed to address the gyroscopic effects inherent in MSR system, such as robust control [22], model-based decoupling control [23], and sliding-mode control [24]. A conventional approach for mitigating gyroscopic effects in MSR system employs decentralized proportional-integral-derivative (PID) control with cross-feedback compensation (PIDCF) [25]-[26]. However, cross-feedback compensation exhibits significant dependence on both PID parameters and rotor speed. The introduction of cross compensation alters the control system dynamics, necessitating readjustment of repetitive controller parameters.

Recent research on enhanced RC includes methods such as a notch filter-based RC [27] and robust adaptive odd-harmonic RC [28]. However, the design in [27] depends on a known and accurately modeled plant to ensure causality and stability of its compensator. The scheme in [28] is limited to rejecting disturbances containing only odd-harmonic components, restricting its applicability to a narrower class of periodic signals. Furthermore, the convergence and stability analysis for the robust adaptive control is notably complex, and its substantial computational burden imposes significant limitations.

The active disturbance rejection controller (ADRC) has gained increasing research interest owing to its strong disturbance rejection performance and model-free characteristics [29]. ADRC has been used in MSR systems to increase robustness [30] and reduce latency [31]. However, its efficacy in achieving reliable decoupling under strong gyroscopic effects remains limited. For example, a prior ADRC-based decoupling method for MSR systems was validated only through simulation, lacking experimental support [32]. Meanwhile, the combination of RC and ADRC has shown promising results in suppressing periodic harmonics in power electronic systems such as permanent magnet synchronous motor drives [33] and grid-tied inverters [34]. Despite this potential, the application and experimental validation of an RC-ADRC strategy specifically for MSR systems under significant gyroscopic effects constitute an unexplored area, which this work aims to address.

To effectively suppress harmonic current caused by unbalanced mass and sensor runout under strong gyroscopic effects, this paper proposes a PC based ADRC scheme to enhance the performance of RC. The main contributions of this work are listed as follows:

1) It proposes an ADRC scheme incorporating an extended state observer (ESO) to estimate and suppress coupling disturbances and sensor noise, achieving decoupled control of the MSR system.

2) A PC is introduced, forming a PC-ADRC that enhances system stability and robust performance through PC.

3) The integrated RC-ADRC scheme is, for the first time, applied and experimentally validated in an MSR system subject to strong gyroscopic effects.

The rest of the paper is organized as follows: Section II presents the dynamic modeling of the MSR system and analyzes internal/external disturbances. Section III details the proposed RC-PCADRC scheme, encompassing the theoretical foundations of RC and ADRC, the design of the controller, and comprehensive stability analysis with parameter optimization. Section IV provides simulation and experimental validation on a 5-degree-of-freedom (DOF) magnetic levitation platform. Finally, conclusions are provided in Section V.

II. Dynamic Model for MSR System and Disturbance Analysis

A. Dynamic Model

The structure of the MSR system is shown in Fig. 1 and the parameters are shown in Table I, in which the rotor is suspended by AMB and PMB. Because the axial and radial degrees of freedom of the rotor are completely decoupled, they are not considered in the model. The AMBs, PMBs, and displacement sensors are symmetrically distributed on both sides of the rotor. The electromagnetic force is determined by the displacement of the rotor and the current of the active

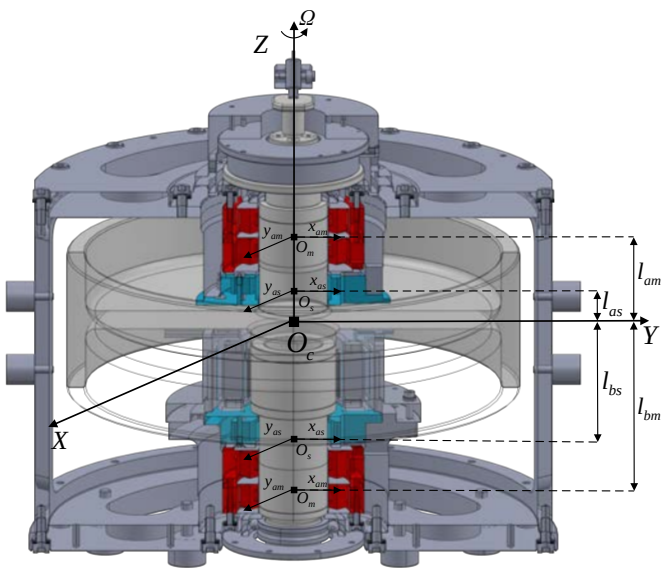

Fig. 1. Diagram of MSR system.

describing rotor motion, namely the rotor center of mass magnetic bearing coil. There are three coordinate systems for coordinate system O_c, the magnetic bearing coordinate system O_m, and the sensor coordinate system O_s. In the three coordinate systems, the rotor coordinate system can be described as $\boldsymbol{q}_c = [\theta_x\ x\ \theta_y\ y]^T$, $\boldsymbol{q}_m = [x_{am}\ x_{bm}\ y_{am}\ y_{bm}]^T$, and $\boldsymbol{q}_s = [x_{as}\ x_{bs}\ y_{as}\ y_{bs}]^T$ in coordinate systems O_c, O_m, and O_s, respectively.

TABLE I
PARAMETERS OF MSR SYSTEM

Parameter	Symbol	Value
Rotor mass	m/kg	9.030
Polar moment of inertia	J_z/(kg·m^2)	0.07459
Transverse moment of inertia	J/(kg·m^2)	0.04632
Distance from 0 to bearing A center	l_{am}/m	0.04734
Distance from 0 to bearing B center	l_{bm}/m	0.08966
Distance from 0 to sensor A center	l_{as}/m	0.02034
Distance from 0 to sensor B center	l_{bs}/m	0.06266
Current stiffness	k_i/(N·A^{-1})	60
Displacement stiffness of AMB	k_{ha}/(N·m^{-1})	2.5×10^5
Displacement stiffness of PMB	k_{hp}/(N·m^{-1})	1.5×10^5
Total displacement stiffness	k_h/(N·m^{-1})	4×10^5
Resistance of AMB coil	R/Ω	0.7
Inductance of AMB coil	L/H	1.5×10^{-3}
Current-loop proportional coefficients	K_{amp}	0.7
Current-loop feedback coefficients	K_f	3
Sensor gain	K_s/(V·m^{-1})	16,000
Sampling time	T_s/s	3×10^{-4}

The conversion relationship between the three coordinate systems can be described as (1):

$$\boldsymbol{q}_c = \boldsymbol{T}_m\boldsymbol{q}_m, \boldsymbol{q}_c = \boldsymbol{T}_s\boldsymbol{q}_s, \boldsymbol{q}_m = \boldsymbol{T}_m^{-1}\boldsymbol{T}_s\boldsymbol{q}_s \tag{1}$$

where

$$\boldsymbol{T}_m = \frac{1}{l_{am}+l_{bm}}\begin{bmatrix} 0 & 0 & 1 & -1 \\ l_{bm} & l_{am} & 0 & 0 \\ -1 & 1 & 0 & 0 \\ 0 & 0 & l_{bm} & l_{am} \end{bmatrix}$$

$$\boldsymbol{T}_s = \frac{1}{l_{as}+l_{bs}}\begin{bmatrix} 0 & 0 & 1 & -1 \\ l_{bs} & l_{as} & 0 & 0 \\ -1 & 1 & 0 & 0 \\ 0 & 0 & l_{bs} & l_{as} \end{bmatrix}$$

The linearized electromagnetic force f_λ in each axis is given by:

$$f_\lambda = k_i i_\lambda + (k_{ha}+k_{hp})h_\lambda, \lambda \in \mathrm{ax, bx, ay, by} \tag{2}$$

where i_λ is the coil current and h_λ is the rotor displacement in coordinate systems O_m. The total displacement stiffness k_h is defined as $k_h = k_{ha} + k_{hp}$. Let Ω denote the rotational speed of the rotor. The dynamic equations of the rotor are:

$$\boldsymbol{M}\ddot{\boldsymbol{q}}_c + \Omega\boldsymbol{G}\dot{\boldsymbol{q}}_c = k_h\boldsymbol{F}\boldsymbol{q}_m + k_i\boldsymbol{i} \tag{3}$$

where

$$\boldsymbol{M} = \begin{bmatrix} J & 0 & 0 & 0 \\ 0 & m & 0 & 0 \\ 0 & 0 & J & 0 \\ 0 & 0 & 0 & m \end{bmatrix}, \boldsymbol{G} = \begin{bmatrix} 0 & 0 & J_z & 0 \\ 0 & 0 & 0 & 0 \\ -J_z & 0 & 0 & 0 \\ 0 & 0 & 0 & 0 \end{bmatrix}$$

$$\boldsymbol{F} = \begin{bmatrix} 0 & 0 & l_{am} & -l_{bm} \\ 1 & 1 & 0 & 0 \\ -l_{am} & l_{bm} & 0 & 0 \\ 0 & 0 & 1 & 1 \end{bmatrix}, \boldsymbol{i} = \begin{bmatrix} i_{ax} & i_{bx} & i_{ay} & i_{by} \end{bmatrix}^T$$

The state variables, controller outputs, and system outputs of the MSR system are defined as the state vector $\boldsymbol{x}$, the control input vector $\boldsymbol{u}$, and the output vector $\boldsymbol{y}$ in the state-space model, respectively. The state vector $\boldsymbol{x}$ includes the rotor displacements at the four radial sensor positions and their corresponding translational velocities, where a dot placed above a displacement variable denotes its first-order time derivative, i.e., velocity. The control input $\boldsymbol{u}$ consists of the coil currents for the four radial axes, and the output $\boldsymbol{y}$ consists of the measured displacements. They are mathematically expressed as:

$$\boldsymbol{x} = \begin{bmatrix} x_{as} & x_{bs} & y_{as} & y_{bs} & \dot{x}_{as} & \dot{x}_{bs} & \dot{y}_{as} & \dot{y}_{bs} \end{bmatrix}^T,$$

$$\boldsymbol{u} = \begin{bmatrix} i_{ax} & i_{bx} & i_{ay} & i_{by} \end{bmatrix}^T, \text{ and } \boldsymbol{y} = \begin{bmatrix} x_{as} & x_{bs} & y_{as} & y_{bs} \end{bmatrix}^T.$$

The state-space model of the MSR system can be written as:

$$\begin{cases} \dot{\boldsymbol{x}} = \boldsymbol{A}\boldsymbol{x} + \boldsymbol{B}\boldsymbol{u} \\ \boldsymbol{y} = \boldsymbol{C}\boldsymbol{x} \end{cases} \tag{4}$$

where

$$\boldsymbol{A} = \begin{bmatrix} 0_{4\times4} & \boldsymbol{I}_{4\times4} \\ \boldsymbol{a}_{4\times4} & \boldsymbol{b}_{4\times4} \end{bmatrix},\ \boldsymbol{B} = \begin{bmatrix} 0_{4\times4} \\ \boldsymbol{c}_{4\times4} \end{bmatrix},\ \boldsymbol{C} = \begin{bmatrix} \boldsymbol{I}_{4\times4} & 0_{4\times4} \end{bmatrix}$$

$$\boldsymbol{a}_{4\times4} = k_h\left(\boldsymbol{M}\boldsymbol{T}_s\right)^{-1}\boldsymbol{F}\boldsymbol{T}_m^{-1}\boldsymbol{T}_s = \begin{bmatrix} k_1 & k_2 & 0 & 0 \\ k_3 & k_4 & 0 & 0 \\ 0 & 0 & k_1 & k_2 \\ 0 & 0 & k_3 & k_4 \end{bmatrix}$$

$$\boldsymbol{b}_{4\times4} = -\Omega\left(\boldsymbol{M}\boldsymbol{T}_s\right)^{-1}\boldsymbol{G}\boldsymbol{T}_s = \begin{bmatrix} 0 & 0 & -k_5 & k_5 \\ 0 & 0 & k_6 & -k_6 \\ k_5 & -k_5 & 0 & 0 \\ -k_6 & k_6 & 0 & 0 \end{bmatrix}$$

$$\boldsymbol{c}_{4\times4} = k_i\left(\boldsymbol{M}\boldsymbol{T}_s\right)^{-1}\boldsymbol{F} = \begin{bmatrix} k_7 & k_8 & 0 & 0 \\ k_9 & k_{10} & 0 & 0 \\ 0 & 0 & k_7 & k_8 \\ 0 & 0 & k_9 & k_{10} \end{bmatrix}$$

$$k_1 = \frac{k_h[J(l_{am}-l_{bm}+2l_{bs})+ml_{as}(l_{am}^{\ 2}+l_{bm}^{\ 2}+l_{bs}l_{am}-l_{bs}l_{bm})]}{Jm(l_{as}+l_{bs})}$$

$$k_2 = \frac{k_h[J(l_{am}-l_{bm}-2l_{as})-ml_{am}l_{as}(l_{am}-l_{as})-ml_{bm}l_{as}(l_{bm}+l_{as})]}{Jm(l_{as}+l_{bs})}$$

$$k_3 = \frac{k_h[J(l_{am}-l_{bm}+2l_{bs})-ml_{am}l_{bs}(l_{am}+l_{bs})-ml_{bm}l_{bs}(l_{bm}-l_{bs})]}{Jm(l_{as}+l_{bs})}$$

$$k_4 = \frac{k_h[J(l_{bm}-l_{am}+2l_{as})+ml_{bs}(l_{am}^{\ 2}+l_{bm}^{\ 2}-l_{as}l_{am}+l_{as}l_{bm})]}{Jm(l_{as}+l_{bs})}$$

$$k_5 = \frac{J_z l_{as}\Omega}{J(l_{as}+l_{bs})}, k_6 = \frac{J_z l_{bs}\Omega}{J(l_{as}+l_{bs})}$$

$$k_7=\frac{k_i}{m}+\frac{k_i l_{\mathrm{am}} l_{\mathrm{as}}}{J}, k_8=\frac{k_i}{m}-\frac{k_i l_{\mathrm{bm}} l_{\mathrm{as}}}{J}$$
$$k_9=\frac{k_i}{m}-\frac{k_i l_{\mathrm{am}} l_{\mathrm{bs}}}{J}, k_{10}=\frac{k_i}{m}+\frac{k_i l_{\mathrm{bm}} l_{\mathrm{bs}}}{J}$$

Within the MSR system, the majority of parameters are known a priori, allowing for direct calculation of all terms except for the rotational speed Ω. With the state-space model that incorporates strong gyroscopic effects now established, the subsequent step involves designing a decoupling control scheme that explicitly accounts for these disturbances.

B. Disturbance Analysis

Based on the above-mentioned state-space (4), and recalling that the double-dot notation signifies acceleration, we can obtain (5) as follows:

$$\begin{cases}\ddot{x}_{\mathrm{as}}=k_1x_{\mathrm{as}}+k_2x_{\mathrm{bs}}-k_5\dot{y}_{\mathrm{as}}+k_5\dot{y}_{\mathrm{bs}}+k_7i_{ax}+k_8i_{\mathrm{bx}}\\ \ddot{x}_{\mathrm{bs}}=k_3x_{\mathrm{as}}+k_4x_{\mathrm{bs}}+k_6\dot{y}_{\mathrm{as}}-k_6\dot{y}_{\mathrm{bs}}+k_9i_{ax}+k_{10}i_{\mathrm{bx}}\\ \ddot{y}_{\mathrm{as}}=k_1y_{\mathrm{as}}+k_2y_{\mathrm{bs}}+k_5\dot{x}_{\mathrm{as}}-k_5\dot{x}_{\mathrm{bs}}+k_7i_{ay}+k_8i_{\mathrm{by}}\\ \ddot{y}_{\mathrm{bs}}=k_3y_{\mathrm{as}}+k_4y_{\mathrm{bs}}-k_6\dot{x}_{\mathrm{as}}+k_6\dot{x}_{\mathrm{bs}}+k_9i_{ay}+k_{10}i_{\mathrm{by}}\end{cases}\tag{5}$$

where each DOF can be composed of a decoupling part and a coupling interference part generated by the gyroscope effect. Separating the decoupling and coupling parts in (5), we can obtain (6) as follows:

$$\begin{cases}\ddot{x}_{\mathrm{as}}=k_{\mathrm{hA}}x_{\mathrm{as}}+k_{\mathrm{iA}}i_{ax}+\eta_{ax}\\ \ddot{x}_{\mathrm{bs}}=k_{\mathrm{hB}}x_{\mathrm{bs}}+k_{\mathrm{iB}}i_{\mathrm{bx}}+\eta_{\mathrm{bx}}\\ \ddot{y}_{\mathrm{as}}=k_{\mathrm{hA}}y_{\mathrm{as}}+k_{i\mathrm{A}}i_{ay}+\eta_{ay}\\ \ddot{y}_{\mathrm{bs}}=k_{\mathrm{hB}}y_{bs}+k_{\mathrm{iB}}i_{by}+\eta_{by}\end{cases}\tag{6}$$

where

$$k_{\mathrm{hA}}=k_{\mathrm{ha}x}=k_{\mathrm{ha}y}=k_1,\ k_{\mathrm{hB}}=k_{\mathrm{hb}x}=k_{\mathrm{hb}y}=k_4$$
$$k_{\mathrm{iA}}=k_{\mathrm{ia}x}=k_{\mathrm{ia}y}=k_7, k_{\mathrm{iB}}=k_{\mathrm{ib}x}=k_{\mathrm{ib}y}=k_{10}$$
$$\eta_{ax}=k_2x_{\mathrm{bs}}-k_5\dot{y}_{\mathrm{as}}+k_5\dot{y}_{\mathrm{bs}}+k_8i_{\mathrm{bx}}$$
$$\eta_{\mathrm{bx}}=k_3x_{\mathrm{as}}+k_6\dot{y}_{\mathrm{as}}-k_6\dot{y}_{\mathrm{bs}}+k_9i_{ax}$$
$$\eta_{ay}=k_2y_{\mathrm{bs}}+k_5\dot{x}_{\mathrm{as}}-k_5\dot{x}_{\mathrm{bs}}+k_8i_{\mathrm{by}}$$
$$\eta_{\mathrm{by}}=k_3y_{\mathrm{as}}-k_6\dot{x}_{\mathrm{as}}+k_6\dot{x}_{\mathrm{bs}}+k_9i_{ay}$$

k_{hA} and k_{hB} are equivalent displacement stiffness of A-AMB and B-AMB, respectively; k_{iA} and k_{iB} are equivalent current stiffness of A-AMB and B-AMB, respectively; η_{ax}, η_{bx}, η_{ay}, and η_{by} represent the disturbances caused by coupling in each DOF, which can be regarded as internal disturbances. The parameters of the equivalent displacement and current stiffness are shown in Table II.

TABLE II
PARAMETERS OF ADRC

Symbol	Value	Symbol	Value
$k_{\mathrm{hA}}/(\mathrm{N\cdot m^{-1}})$	6.044×10^4	$k_{\mathrm{hB}}/(\mathrm{N\cdot m^{-1}})$	11.69×10^4
$k_{\mathrm{iA}}/(\mathrm{N\cdot A^{-1}})$	7.892	$k_{\mathrm{iB}}/(\mathrm{N\cdot A^{-1}})$	13.92

It can be seen from [19] that the mass unbalance can be regarded as synchronous disturbances, and the sensor runout causes harmonic disturbances. Therefore, the external disturbances of the MSR system can be expressed as (7):

$$\begin{cases}\omega_{ax}=d_{\mathrm{a}}\cos\left(\Omega t+\varphi_{\mathrm{a}}\right)+\sum_{i=1}^{+\infty}c_{axi}\cos\left(i\Omega t+\alpha_{axi}\right)\\ \omega_{\mathrm{bx}}=d_{\mathrm{b}}\cos\left(\Omega t+\varphi_{\mathrm{b}}\right)+\sum_{i=1}^{+\infty}c_{\mathrm{bx}i}\cos\left(i\Omega t+\alpha_{\mathrm{bx}i}\right)\\ \omega_{ay}=d_{\mathrm{a}}\sin\left(\Omega t+\varphi_{\mathrm{a}}\right)+\sum_{i=1}^{+\infty}c_{ayi}\cos\left(i\Omega t+\alpha_{ayi}\right)\\ \omega_{\mathrm{by}}=d_{\mathrm{b}}\sin\left(\Omega t+\varphi_{\mathrm{b}}\right)+\sum_{i=1}^{+\infty}c_{\mathrm{by}i}\cos\left(i\Omega t+\alpha_{\mathrm{by}i}\right)\end{cases}\tag{7}$$

where ω_{ax}, ω_{bx}, ω_{ay}, and ω_{by} are the external disturbances caused by a combination of mass imbalance and sensor runout. d_{a} and d_{b} are the amplitude of the disturbances caused by mass imbalance at A-AMB and B-AMB, φ_{a} and φ_{b} are the initial phase of the disturbance caused by mass imbalance at A-AMB and B-AMB; i is the number of harmonics (i = 1, 2, 3,…), c_{axi}, $c_{\mathrm{bx}i}$, c_{ayi}, and $c_{\mathrm{by}i}$ are the amplitude of the ith harmonic caused by sensor runout, α_{axi}, $\alpha_{\mathrm{bx}i}$, α_{ayi}, and $\alpha_{\mathrm{by}i}$ are the initial phase of the ith harmonic caused by sensor runout; t denotes time.

Therefore, for each degree of freedom, and noting that the double-dot notation denotes the acceleration, the decoupling equation can be written as (8):

$$\ddot{h}_\lambda=k_{h_\lambda}h_\lambda+k_{i_\lambda}i_\lambda+\eta_\lambda+\omega_\lambda,\lambda\in\mathrm{ax},\mathrm{bx},\mathrm{ay},\mathrm{by}\tag{8}$$

The above analysis reveals that in the decoupling control of the MSR system, disturbances can be categorized into internal disturbances (induced by gyroscopic effects) and external disturbances (resulting from mass imbalance and sensor runout). While repetitive controllers effectively attenuate external disturbances, their inability to suppress internal disturbances limits overall control performance. Thus, a comprehensive control strategy must account for both disturbance types.

III. DESIGN AND ANALYSIS OF RC-ADRC

To suppress internal and external disturbances simultaneously, this section proposes an RC-PCADRC scheme for MSR system. Fig. 2 depicts the block diagram of the decoupling model of MSR system with the proposed scheme. $G_{\mathrm{p}}(s)$ represents the transfer function of the decoupled MSR system, accounting for both internal and external disturbances. K_{s} is the gain of sensor. $P(s)$ represents the transfer function of PC. By cascading an ESO with $P(s)$, the dynamic response capability of ADRC is improved, and the speed of disturbance observation is enhanced with reduced noise sensitivity. A modified plug-in RC is proposed in [16], with its transfer function represented as $G_{\mathrm{rc}}(s)$. The basic principle of the controller is illustrated schematically below. $G_{\mathrm{LPF}}(s)$ represents the low-pass filter (LPF). The transfer function $G_{\mathrm{LPF}}(s)$ of a first-order LPF can be expressed as (9):

$$G_{\mathrm{LPF}}(s)=\frac{\omega_{\mathrm{LPF}}}{s+\omega_{\mathrm{LPF}}}\tag{9}$$

where ω_{LPF} denotes the cutoff frequency. Set ω_{LPF} = 3142 rad/s.

In this study, attention is directed toward the displacement

controller. The current loop is modeled as a first-order inertial element governed by its bandwidth, and it can be represented as the transfer function $G_w(s)$:

$$\begin{cases} G_w(s) = \dfrac{K_w}{s/\omega_b + 1} \\ K_w = \dfrac{K_{amp}}{R + K_{amp}K_f} \\ \omega_b = \dfrac{R + K_{amp}K_f}{L} \end{cases} \tag{10}$$

where ω_b is the current loop bandwidth, and K_w is the closed-loop gain. Here, R and L are the resistance and inductance of the AMB coil, K_{amp} is the gain of the power amplifier, and K_f is the current feedback coefficient, as defined in Table I.

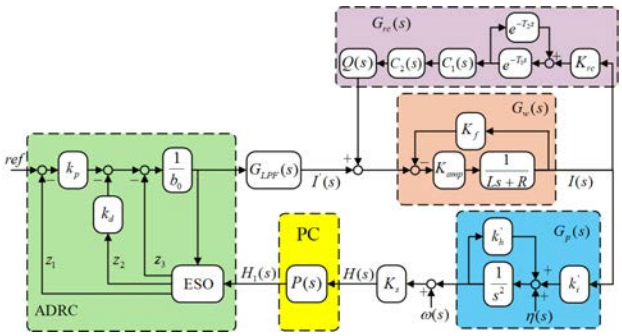

Fig. 2. Block diagram of the decoupling model with RC-PCADRC.

A. Theory of RC

RC based on the internal model principle effectively suppresses current harmonics by embedding a periodic signal generator in the control loop, ensuring precise tracking and rejection of periodic disturbances. $Q(s)$ is an LPF, whose cutoff frequency ω_q is set to 3142 rad/s. $C_1(s)$ and $C_2(s)$ are the phase compensators for the low and medium frequency bands of the RC, respectively. $e^{-T_1 s}$ and $e^{-T_2 s}$ are the time-delay element. T is the total system delay time, where $T = T_1 + T_2$, $T_1 = N_1 T_s$, and $T_2 = N_2 T_s$. $e^{-T_1 s}$ and $e^{-T_2 s}$ are responsible for the PC in the high-frequency band of the RC. K_{rc} denotes the gain of the RC. A larger value accelerates the disturbance rejection speed of the RC controller; however, excessively high K_{rc} may compromise system stability. According to Fig. 2, the transfer function of plug-in RC is (11):

$$G_{rc}(s) = \frac{K_{rc}Q(s)C_1(s)C_2(s)e^{-Ts}e^{T_2 s}}{1 - e^{-Ts}} \tag{11}$$

The sensitivity function $S(s)$, which relates the output current $I(s)$ to the combined reference and disturbance input, can be expressed as (12):

:

$$\begin{aligned} S(s) &= \frac{I(s)}{\text{ref} - K_s\omega(s)} \\ &= \frac{(1 - e^{-Ts})S_0(s)}{1 - \left[1 + \dfrac{S_0(s)K_{rc}Q(s)C_1(s)C_2(s)e^{T_2 s}}{G_c(s)G_{LPF}(s)}\right]e^{-Ts}} \end{aligned} \tag{12}$$

where $S_0(s) = \dfrac{G_c(s)G_{LPF}(s)G_w(s)}{1 + G_c(s)G_{LPF}(s)G_w(s)G_p(s)K_s}$ is the sensitivity function of original system without RC. $G_c(s)$ is the displacement controller.

As $T = 2\pi\Omega$, $|e^{-Ts}|_{s=j\omega} = 1$ and $\arg(e^{-Ts})_{s=j\omega} = -2n\pi$ when the frequency of $[\text{ref} - K_s\omega(s)]_{s=j\omega}$ approaches $\omega_n = n\Omega$ (n = 1, 2, 3,…). Thus, $S(s) = 0$, indicating that the influence of external disturbances on the current is fully suppressed.

The closed-loop characteristic equation can be expressed as (13):

$$M(s) - e^{-Ts}N(s) = 0 \tag{13}$$

where

$$N(s) = 1 + G_w(s)\left[G_c(s)G_{LPF}(s)G_p(s)K_s + K_{rc}Q(s)C(s)e^{T_2 s}\right]$$
$$M(s) = 1 + G_c(s)G_{LPF}(s)G_w(s)G_p(s)K_s$$

According to [18], the regeneration spectrum $R(\omega)$ can be defined as:

$$\begin{aligned} R(\omega) &= \left|\frac{N(s)}{M(s)}\right|_{s=j\omega} \\ &= \left|1 + \frac{K_{rc}G_w(s)Q(s)C(s)e^{T_2 s}}{1 + G_c(s)G_{LPF}(s)G_w(s)G_p(s)K_s}\right|_{s=j\omega} \end{aligned} \tag{14}$$

If the original system without RC is stable and $R(\omega) < 1$, the closed-loop system in Fig. 2 is stable.

Equation (14) indicates that the stability of system in Fig. 2 depends not only on the RC design but also on the model parameters of original system and transfer function of controller $G_c(s)$. Coupling disturbances increase model parameter uncertainty, degrading the effectiveness of phase compensator and consequently impairing RC performance. ADRC enables effective disturbance suppression under decoupling control, which is essential to enhance RC efficacy.

B. Theory of Conventional ADRC and Regular Design

Based on the ADRC principle [35], and with the notation that a dot denotes a first-order time derivative, (8) can be reformulated as the following extended state equation:

$$\begin{cases} \begin{bmatrix} \dot{h}_\lambda \\ \dot{v}_\lambda \\ \dot{\delta}_\lambda \end{bmatrix} = \boldsymbol{A}_e \begin{bmatrix} h_\lambda \\ v_\lambda \\ \delta_\lambda \end{bmatrix} + \boldsymbol{B}_e i_\lambda + \boldsymbol{E}_e l_\lambda \\ h_\lambda = \boldsymbol{C}_e \begin{bmatrix} h_\lambda \\ v_\lambda \\ \delta_\lambda \end{bmatrix} \end{cases} \tag{15}$$

where

$$\boldsymbol{A}_e = \begin{bmatrix} 0 & 1 & 0 \\ 0 & 0 & 1 \\ 0 & 0 & 0 \end{bmatrix},\ \boldsymbol{B}_e = \begin{bmatrix} 0 \\ b_0 \\ 0 \end{bmatrix},\ \boldsymbol{E}_e = \begin{bmatrix} 0 \\ 0 \\ 1 \end{bmatrix},\ \boldsymbol{C}_e = \begin{bmatrix} 1 & 0 & 0 \end{bmatrix}$$

where $\lambda \in ax, bx, ay, by$; l_λ is the change rate of δ_λ, $\delta_\lambda = \eta_\lambda + k'_h\omega_\lambda$; b_0 is the control gain.

According to (15), ESO can be designed as [36]:

$$\begin{cases} \dot{\boldsymbol{z}} = \left(\boldsymbol{A}_{\mathrm{e}} - \boldsymbol{L}_{\mathrm{e}}\boldsymbol{C}_{\mathrm{e}}\right)z + \boldsymbol{B}_{\mathrm{e}}i_{\lambda} + \boldsymbol{L}_{\mathrm{e}}h_{\lambda} \\ u_0 = \mathrm{ref} - \begin{bmatrix}\boldsymbol{K}_0 & 1\end{bmatrix}z \end{cases} \tag{16}$$

where

$$\boldsymbol{z} = \begin{bmatrix} z_1 & z_2 & z_3 \end{bmatrix}^{\mathrm{T}},\ \boldsymbol{L}_{\mathrm{e}} = \begin{bmatrix} \beta_1 & \beta_2 & \beta_3 \end{bmatrix}^{\mathrm{T}},\ \boldsymbol{K}_0 = \begin{bmatrix} k_{\mathrm{p}} & k_{\mathrm{d}} \end{bmatrix}$$

z_1, z_2, and z_3 are the observed values of h_λ, v_λ, and δ_λ, respectively; β_1, β_2, and β_3 are the gains of ESO; $\boldsymbol{K}_0$ is the control law of ADRC, while k_{p} and k_{d} are the parameters of the PD controller.

With known plant information, the characteristic equation of ESO is:

$$\left|s\boldsymbol{I}_{3\times3} - \left(\boldsymbol{A}_{\mathrm{e}} - \boldsymbol{L}_{\mathrm{e}}\boldsymbol{C}_{\mathrm{e}}\right)\right| = s^3 + \beta_1 s^2 + \beta_2 s + \beta_3 \tag{17}$$

To place the poles of the ESO eigenvalue at $-\omega_0$, the following condition must hold:

$$\begin{cases} \beta_1 = 3\omega_0 \\ \beta_2 = 3\omega_0^2 \\ \beta_3 = \omega_0^3 \end{cases} \tag{18}$$

where ω_0 represents bandwidth of ESO.

The control block diagram of ADRC is shown in Fig. 3. The expected response characteristic equation is:

$$\lambda(s) = s^2 + k_{\mathrm{d}}s + k_{\mathrm{p}} \tag{19}$$

To place the poles of the control law eigenvalue at $-\omega_{\mathrm{c}}$, the following condition must hold:

$$\begin{cases} k_{\mathrm{p}} = \omega_{\mathrm{c}}^2 \\ k_{\mathrm{d}} = 2\xi\omega_{\mathrm{c}} \end{cases} \tag{20}$$

where ξ is the control law damping ratio, ω_{c} represents controller bandwidth. Setting ξ = 1 in this article, the characteristic equation satisfies $\lambda(s) = (s + \omega_{\mathrm{c}})^2$.

According to (15) and (16), the block diagram of Fig. 3 can be simplified as Fig. 4. $G_1'(s)$ and $G_2'(s)$ can be obtained as (21) and (22):

$$G_1'(s) = \frac{\omega_0\left(s\omega_0 + \omega_{\mathrm{c}}\right)\left[s\left(s\omega_0 + \omega_{\mathrm{c}}\right) + \omega_0\omega_{\mathrm{c}}\right]}{b_0 s\left[\left(s+\omega_0\right)\left(s+3\omega_0+2\omega_{\mathrm{c}}\right) + \omega_{\mathrm{c}}\left(3\omega_0+\omega_{\mathrm{c}}\right)\right]} \tag{21}$$

$$G_2'(s) = \frac{\omega_{\mathrm{c}}^2\left(s+\omega_0\right)^3}{b_0 s\left[\left(s+\omega_0\right)\left(s+3\omega_0+2\omega_{\mathrm{c}}\right) + \omega_{\mathrm{c}}\left(3\omega_0+\omega_{\mathrm{c}}\right)\right]} \tag{22}$$

For the AMB system, the reference value ref = 0. The transfer function of ADRC is $G_1'(s)$.

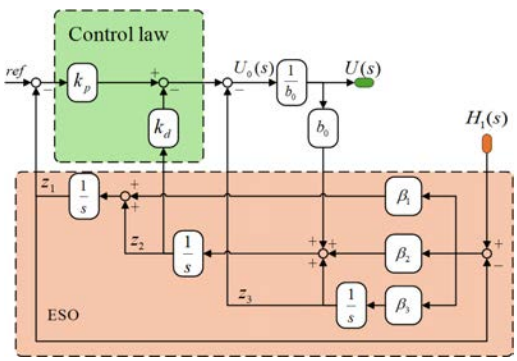

Fig. 3. Block diagram of conventional ADRC.

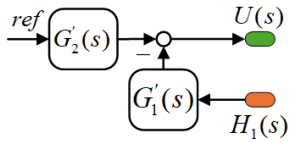

Fig. 4. Simplified block diagram of conventional ADRC.

Equation (21) indicates that the control performance of ADRC is characterized by three key parameters: ω_0, ω_{c}, and b_0.

Firstly, set b_0. Since $k_{\mathrm{iA}} \neq k_{\mathrm{iB}}$, set $b_{0\mathrm{A}}$ and $b_{0\mathrm{B}}$ as the control gain of A-AMB and B-AMB, respectively. Due to the amplification of disturbances by the sensor gain and amplifier, the ADRC gain must be proportionally increased by the K_{s} and K_{w}. Consequently, $b_{0\mathrm{A}} = k_{\mathrm{iA}} \times K_{\mathrm{s}} \times K_{\mathrm{w}}$, and $b_{0\mathrm{B}} = k_{\mathrm{iB}} \times K_{\mathrm{s}} \times K_{\mathrm{w}}$.

Then, set ω_0. According to (16), the transfer function of disturbances estimation can be expressed as (23):

$$G_{z_3\delta}(s) = \frac{z_3}{\delta} = \frac{\omega_0^3}{\left(s+\omega_0\right)^3} \tag{23}$$

Fig. 5 shows the magnitude-frequency characteristic curves of $G_{z_3\delta}(s)$ with different ω_0. Increasing the bandwidth of the ESO enhances its ability to detect higher-frequency disturbances. However, an excessively high ω_0 may unduly amplify the impact of high-frequency noise, increase computational load, and compromise system robustness [32]. For the harmonics in (7), the case where $i \leq 5$ is considered. As the maximum rotational speed is 3000 r/min (314.2 rad/s), the highest-frequency harmonic that needs to be observed is the 5th-order harmonic, corresponding to a frequency of 1570.8 rad/s. To provide a 20% engineering margin, ω_0 is set to 1800 rad/s.

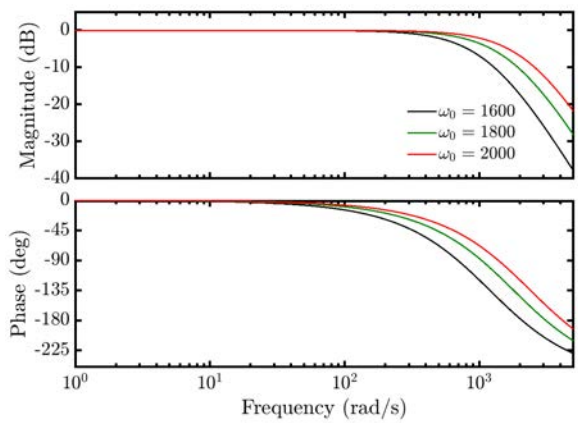

Fig. 5. Bode plot of $G_{z_3\delta}(s)$ with varying ω_0.

Finally, set ω_{c}. Based on engineering practice, the relation $3\omega_{\mathrm{c}} \leq \omega_0 \leq 5\omega_{\mathrm{c}}$ is generally maintained. Given the negative displacement stiffness of the magnetic bearing, a higher control gain is required. Therefore, ω_{c} is set to 550 rad/s.

C. PC Design

After designing the ADRC, its performance was found to be insufficient for stability due to the large negative displacement stiffness of the MSR system. The open-loop transfer function of the ADRC with a decoupled model can be obtained as (24):

$$G_{\mathrm{o}}^{\mathrm{ADRC}}(s)=G_1'(s)G_{\mathrm{LPF}}(s)G_{\mathrm{w}}(s)G_{\mathrm{p}}(s)K_{\mathrm{s}} \tag{24}$$

The Bode plot derived from (24) is presented in Fig. 6(a), indicating system instability due to an insufficient phase margin in the low-frequency region. To address this issue, a PC is designed to augment the phase margin, thereby improving closed-loop stability. With a and b denoting the compensator parameters, the PC is implemented as (25):

$$P(s)=\frac{s+a}{s+b}=\frac{a}{b}\frac{1+s/a}{1+s/b} \tag{25}$$

To compensate for low frequencies, set $b > a$. When $\omega \gg b$, $|P(s)|_{s=j\omega} = 1$ and $\arg[P(s)]_{s=j\omega} = 0$. Therefore, $P(s)$ provides targeted compensation in the low-frequency range while maintaining the performance of high-frequency dynamics.

The maximum phase lead $\phi_{\max}$ introduced by $P(s)$, which occurs at the center frequency ω_{m}, is given by:

$$\phi_{\max}=\arg_{\omega_{\mathrm{m}}=\sqrt{ab}}\left[P(j\omega)\right]=\arcsin\left(\frac{b-a}{b+a}\right) \tag{26}$$

Figs. 6(b) and 6(c) illustrate the compensated open-loop Bode diagrams under different values of ω_{m} and $\phi_{\max}$, respectively. The following observations can be made:

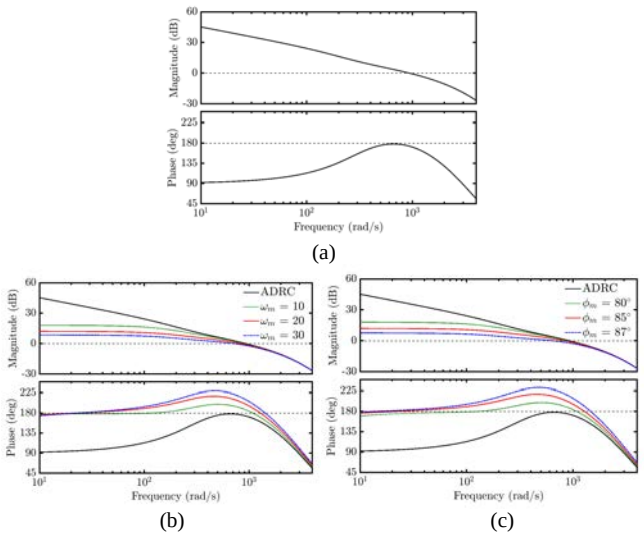

Fig. 6 ADRC open-loop frequency response. (a) No compensation. (b) Varied ω_{m}. (c) Varied $\phi_{\max}$.

With a fixed $\phi_{\max}$, increasing ω_{m} improves the phase margin, but an excessively high ω_{m} leads to insufficient low-frequency gain, while a very low ω_{m} results in an inadequate phase margin and reduced stability.

With a fixed ω_{m}, a higher $\phi_{\max}$ enhances the stability margin, but an overly high $\phi_{\max}$ also reduces the low-frequency gain, whereas a very low $\phi_{\max}$ yields an insufficient phase margin, exhibiting a trade-off similar to that of ω_{m}.

Considering these trade-offs comprehensively, $\omega_{\mathrm{m}} = 20$ and $\phi_{\max} = 85°$ are selected in this work. It can be calculated that $a = 0.8732$, $b = 458.1$.

The dominant root locus plot is illustrated in Fig. 7, with the rotational frequency sweeping from 0 to 50 Hz at 5 Hz intervals. All system poles lie strictly in the left half-plane without RC implementation. Therefore, the MSR system is stable with PCADRC.

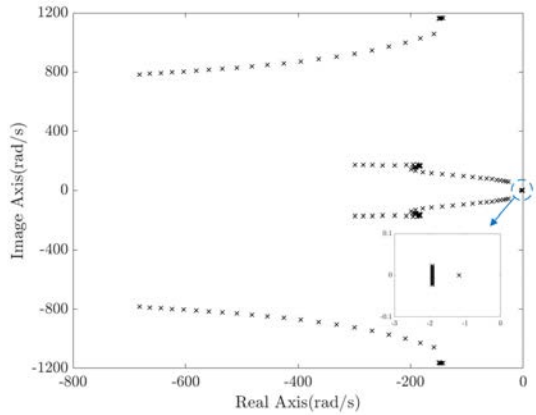

Fig. 7. Closed-loop dominant root locus plot with PCADRC.

D. PC for RC Design

With the PCADRC designed and its transfer function established as $G_{\mathrm{c}}(s) = G_1'(s)P(s)$, the phase compensator $C(s)$ and parameters T_1 and T_2 for the RC in (14) are then designed following the description in [16] to satisfy $R(\omega) < 1$.

By employing PCADRC to suppress the gyroscopic effect, the MSR system can be controlled as an approximately decoupled model, which effectively mitigates the decoupling disturbance acting on the RC controller. PC for the RC controller is subsequently required.

Defining:

$$F(s)=\frac{G_{\mathrm{LPF}}(s)}{1+G_{\mathrm{c}}(s)G_{\mathrm{LPF}}(s)G_{\omega}(s)G_{\mathrm{p}}(s)K_{\mathrm{s}}}=K(\omega)e^{j\theta(\omega)} \text{ and}$$

$$C(s)\big|_{s=j\omega}=K_{\mathrm{c}}(\omega)e^{j\theta_{\mathrm{c}}(\omega)}$$

In the case with $\omega < \omega_{\mathrm{q}}$, the stability criterion of RC in (14) can be rewritten as:

$$\left|1+K_{\mathrm{rc}}K(\omega)K_{\mathrm{c}}(\omega)e^{j[\theta(\omega)+\theta_{\mathrm{c}}(\omega)+T_2\omega]}\right|_{s=j\omega}<1 \tag{27}$$

Set $\varphi(\omega) = \theta(\omega) + \theta_{\mathrm{c}}(\omega) + T_2\omega$. Since $K(\omega) > 0$ and $K_{\mathrm{c}}(\omega) > 0$, to satisfy (25), the phase must satisfy:

$$90°<\varphi(\omega)<270° \tag{28}$$

To achieve a larger value of K_{rc}, $\varphi(\omega)$ should close to 180°.

According to [16], PC is achieved by a proportional-integral (PI) controller in the low-frequency region and by $e^{T_2 s}$ in the high-frequency region.

The PI controller is formulated as (29):

$$C_1(s)=\frac{s+1}{s} \tag{29}$$

For high-frequency phase enhancement, the value of N_2 is set to 4.

An enhanced band-pass filter is proposed for mid-frequency PC, expressed as:

$$C_2(s)=\frac{\omega_{\mathrm{p}}}{\omega_{\mathrm{z}}}\frac{s^2+2\zeta\omega_{\mathrm{z}}s+\omega_{\mathrm{z}}^2}{s^2++2\zeta\omega_{\mathrm{p}}s+\omega_{\mathrm{p}}^2} \tag{30}$$

where ω_{p} represents the angular pole frequency, ω_{z} denotes the angular zero frequency, and ζ denotes the damping ratio controlling the response sharpness and phase characteristics. To ensure symmetric gain distribution around the peak

response frequency, the center frequency ω_{c0} is geometrically determined as:

$$\omega_{c0} = \sqrt{\omega_z \omega_p} \tag{31}$$

Based on the frequency of maximum phase lag (1400 rad/s), ω_{c0} is set accordingly, resulting in these parameters: ω_p = 2000 rad/s, ω_z = 980 rad/s, and ζ = 0.4.

As shown in Fig. 8, the Bode plots before and after PC are presented. It can be observed that for $F(s)$, the PC strategy proposed in this section effectively corrects the phase response without introducing significant magnitude amplification.

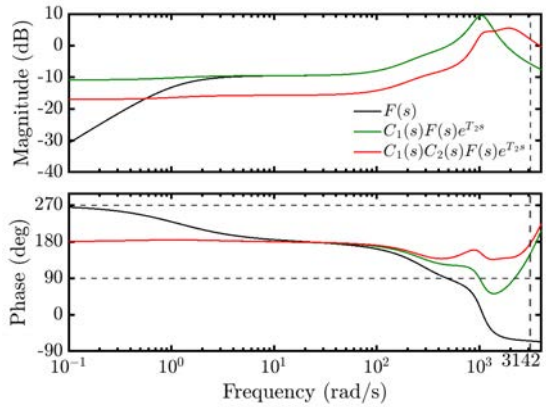

Fig. 8. Bode plot of $F(s)$, $C_1(s)F(s)e^{T_2 s}$, and $C_1(s)C_2(s)F(s)e^{T_2 s}$.

With K_{rc} selected as 0.1, the sensitivity function $S(s)$ of the conventional ADRC and the proposed RC-PCADRC are compared in Fig. 9. The results demonstrate that the RC effectively suppresses high-frequency noise, complementing the ADRC, while the PC successfully reduces the peak value of the sensitivity function, thereby enhancing robustness.

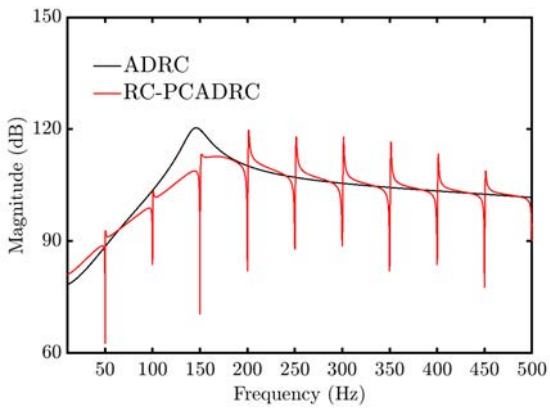

Fig. 9. Comparison of sensitivity functions $S(s)$ for the ADRC and the proposed RC-PCADRC.

IV. Simulation and Experimental Verification

To validate the effectiveness of the proposed scheme in suppressing current harmonics, both simulations and experiments were carried out on the MSR system experimental platform outlined in Table I. Comparison between the proposed RC-PCADRC and the method is proposed in [16].

Considering that the actual system is controlled by a discrete-time controller, the Tustin method is employed to discretize the controller for both simulation and experimental implementation. In cases where the delay order must be an integer, a second-order fractional delay approximation is applied, expressed as:

$$z^{-F} = \sum_{r=0}^{2} m_r z^{-r} \tag{32}$$

where $m_r = \prod_{p=0, p\neq r}^{2} \frac{F-p}{r-p}$.

Here, F is the fractional delay order to be approximated; r and p are integer indices running from 0 to 2; m_r are the coefficients of the second-order approximation.

A. Simulation Results

Fig. 10 shows the simulation results of the coil current without/with RC, employing different control schemes.

In Fig. 10(a), the coil current amplitude measures approximately 1.4 A using PCADRC without RC, which is reduced to 0.4 A after employing the PCADRC + RC strategy. In Fig. 10(b), the coil current amplitude measures approximately 1.6 A using PIDCF without RC, which declines to 0.8 A with the PIDCF + RC scheme.

A comparison between Figs. 10(a) and 10(b) conclusively demonstrates that the PCADRC-based scheme achieves more effective harmonic current suppression than its PIDCF-based scheme.

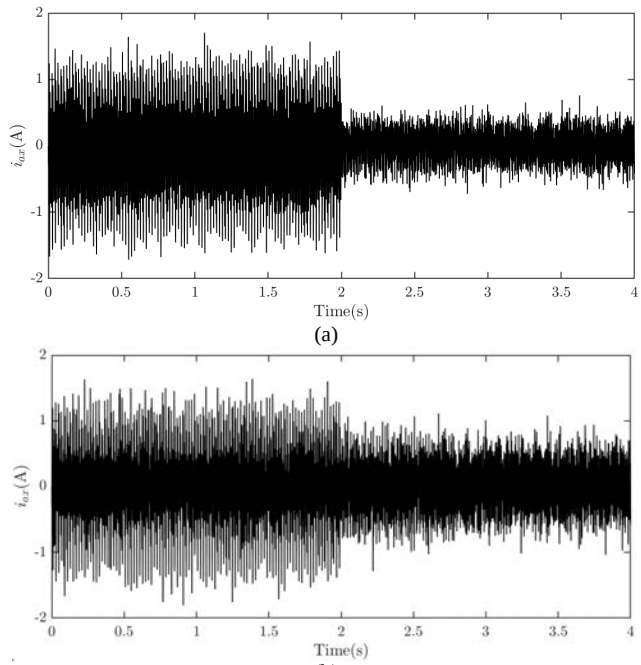

Fig. 10. Simulation results of the coil current at 3000 r/min. (a) PCADRC without/with RC. (b) PIDCF without/with RC.

B. Experimental Setup

To validate the effectiveness of the proposed control strategy, experiments were carried out on a five-degree-of-freedom hybrid magnetic levitation bearing test platform, as illustrated in Fig. 11.

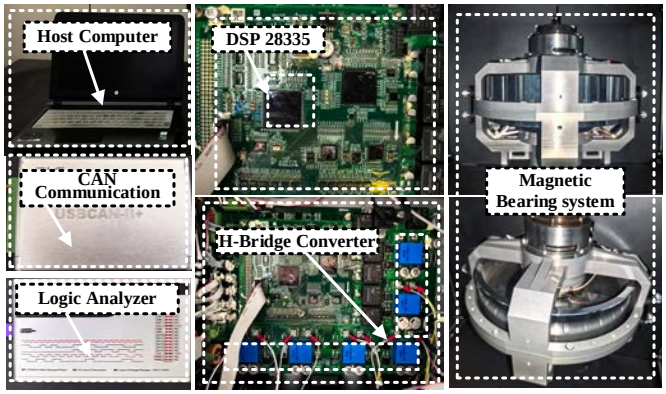

Fig. 11. Experimental platform.

A hardware controller utilizing a TMS320F28335 digital signal processor (DSP) was employed to implement the control algorithm. The pulse width modulation (PWM) switching frequency was configured to 20 kHz, with a direct current (DC) bus voltage of 36 V. The experiments were conducted via a host computer, and data acquisition was performed using a logic analyzer. Communication between the host computer and the DSP within the magnetic bearing platform was achieved through CAN protocol.

C. Experimental Results

To verify the harmonic suppression effect of the proposed RC-PCADRC scheme, tests were conducted at a rotor speed of 3000 r/min. Fig. 12 compares the current i_{ax} waveforms of the proposed PCADRC scheme and PIDCF scheme without/with RC. In Fig. 12(a), the PCADRC current measures 1.5 A without RC compensation. After introducing RC compensation, the current decreases from 1.5 to 0.4 A. In Fig. 12(b), the PIDCF current measures 1.5 A without RC compensation. After introducing RC compensation, the current decreases from 1.5 to 0.6 A. A comparative analysis of the experimental results reveals the superior efficacy of the proposed RC-PCADRC scheme over the PIDCF + RC method in suppressing current harmonics.

Fig. 13 presents the harmonic spectra under the PIDCF without/with RC, and PCADRC without/with RC, respectively. Figs. 13(a) and 13(b) show that the implementation of the PIDCF + RC scheme improved the attenuation of the first to fifth harmonic orders by 9.4 dB (−31.9 to −41.3 dB), 6.6 dB (−40.6 to −47.2 dB), 8.6 dB (−42.8 to −51.4 dB), 9.9 dB (−38.9 to −48.8 dB), and 6.3 dB (−35.0 to −41.3 dB), respectively. In comparison, Figs. 13(c) and 13(d) show that the RC-PCADRC scheme achieved greater improvements of 18.0 dB (−36.3 to −54.3 dB), 15.0 dB (−38.3 to −53.3 dB), 14.8 dB (−38.3 to −53.1 dB), 14.6 dB (−38.2 to −52.8 dB), and 17.3 dB (−32.8 to −50.1 dB), respectively. The comparative analysis confirms the superior performance of the proposed RC-PCADRC scheme, as it attains significantly higher final attenuation levels across all harmonic orders. Although the suppression capability of RC diminishes for harmonic noise above 300 Hz, the amplitude of such noise is negligible (below −45 dB). Consequently, the design focuses primarily on the 1st to 5th harmonics.

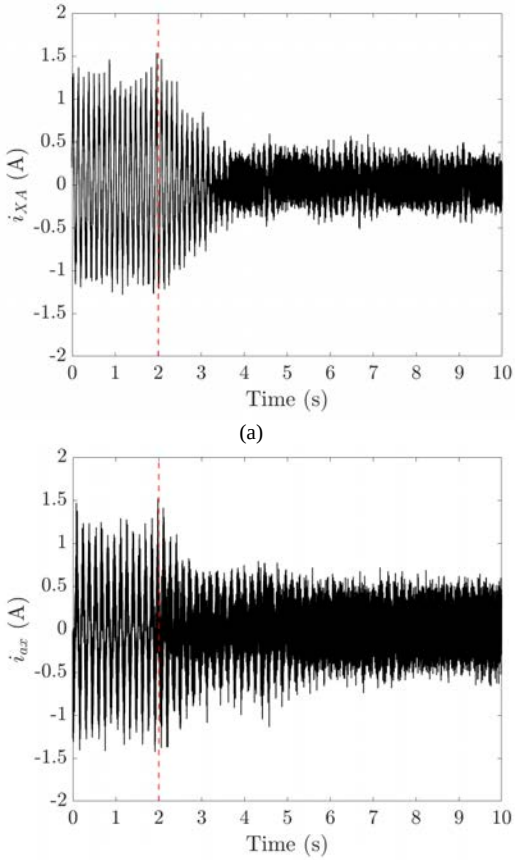

Fig. 12. Experimental results of the coil current i_{ax} at 50 Hz. (a) Modified ADRC without/with RC. (b) PIDCF without/with RC.

Rotor motion was measured in the two radial bearing planes, with the vibration amplitude denoted as r. Fig. 14 illustrates the rotor displacement performance at bearings A and B under different control schemes. As shown in Fig. 14(a), the use of PIDCF resulted in vibration amplitudes of 32 μm at the A-end and 32 μm at the B-end. With the addition of RC, as presented in Fig. 14(b), the vibration amplitudes decreased to 20 μm at the A-end and 18 μm at the B-end. When PCADRC was implemented individually (Fig. 14(c)), the corresponding amplitudes were 25 μm at the A-end and 30 μm at the B-end. Finally, under the combined RC-PCADRC scheme in Fig. 14(d), the rotor displacement was further reduced to 10 μm at both the A-end and B-end. The superior suppression of harmonic current achieved by the RC-PCADRC scheme, as shown in Fig. 14, directly leads to a reduction in harmonic vibration forces. This force reduction is the key factor enabling stable rotor operation with the lower displacement amplitudes, demonstrating a significant improvement in rotational precision.

V. CONCLUSION

In order to effectively suppress harmonic current in MSR systems under strong gyroscopic effects, this paper proposes a novel control scheme that integrates RC with PC-based ADRC. The proposed scheme effectively combines the complementary advantages of repetitive control for periodic

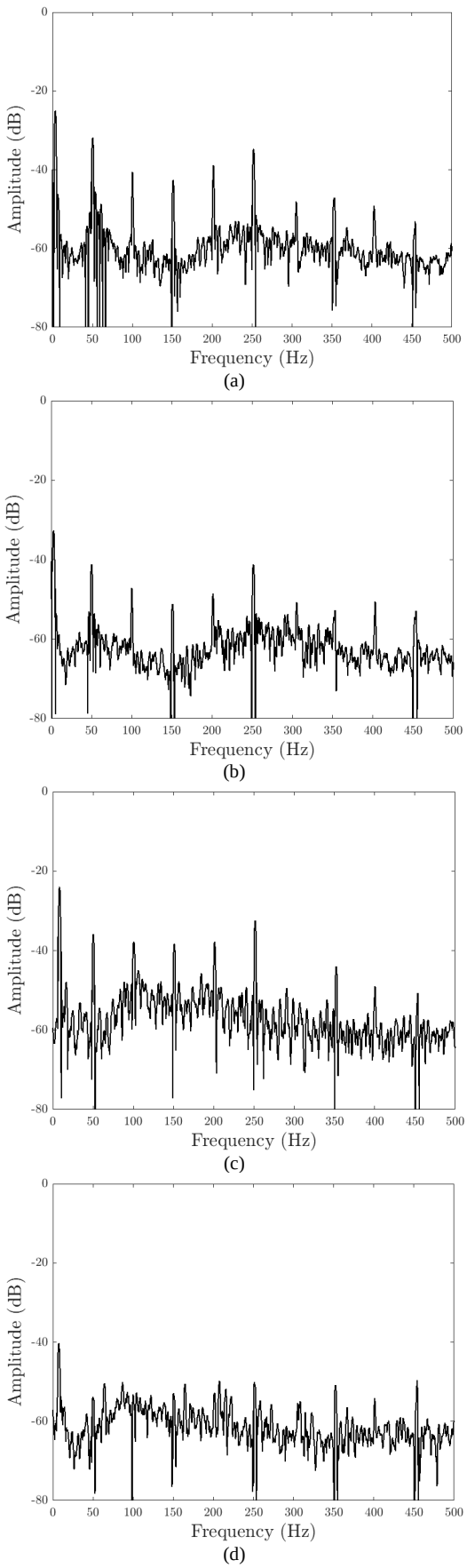

Fig. 13. Experimental frequency spectrum of coil current i_{ax} at 50 Hz. (a) PIDCF. (b) PIDCF with RC. (c) PCADRC. (d) RC-PCADRC.

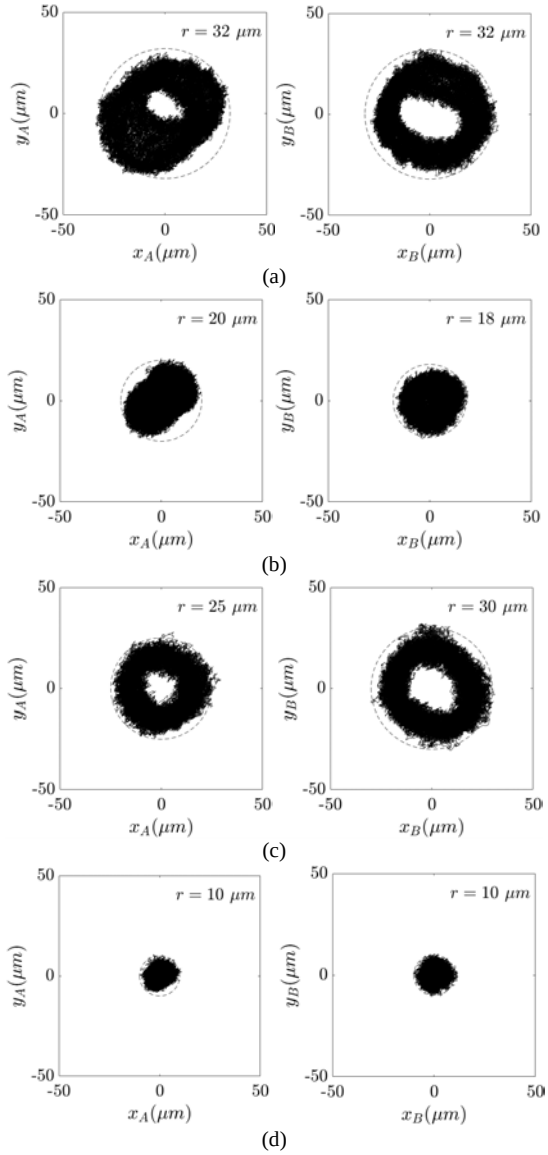

Fig. 14. Experimental results of measured rotor motion in the two radial bearing planes at 50 Hz. (a) PIDCF. (b) PIDCF with RC. (c) PCADRC. (d) RC-PCADRC.

disturbance suppression and ADRC for robust estimation of internal disturbances. A key contribution lies in the incorporation of the phase compensator, which specifically addresses the low-frequency phase lag inherent in conventional ADRC implementations. This enhancement significantly improves both the accuracy and robustness of the decoupling model, thereby establishing a more reliable foundation for the subsequent repetitive controller design. Simulation and experimental results obtained from a five-degree-of-freedom magnetic levitation platform demonstrate the scheme's superior performance in harmonic attenuation and rotor vibration suppression. The proposed control strategy offers substantial practical value for high-precision magnetic bearing applications, particularly in enhancing rotational accuracy, improving system stability, and extending operational lifespan in demanding industrial environments. Particularly, it shows critical potential for hydro turbines, enhancing their operational reliability and longevity under

demanding operating conditions. Furthermore, future work will explore the impact of both speed fluctuations and temperature variations on system parameters, along with the development of corresponding adaptive mechanisms to enhance the control scheme's robustness under a wider range of operating conditions.

REFERENCES

[1] E. H. Maslen, and G. Schweitzer, *Magnetic Bearings: Theory, Design, and Application to Rotating Machinery*. Berlin, Heidelberg: Springer, 2009.

[2] J. H. Ye, D. Shi, and Y. S. Qi *et al*., "Vibration Suppression for Active Magnetic Bearings Using Adaptive Filter with Iterative Search Algorithm," *CES Transactions on Electrical Machines and Systems*, vol. 8, no. 1, pp. 61–71, Mar. 2024.

[3] Y. F. Yin, X. M. Liu, and K. Wang *et al*., "Self-identification and Balancing for AMB-rotor System of Turbomolecular Pumps," *IEEE/ASME Transactions on Mechatronics*, vol. 30, no. 3, pp. 2028–2037, Jun. 2025.

[4] H. B. Sun, D. Jiang, and J. C. Yang, "Synchronous Vibration Suppression of Magnetic Bearing Systems without Angular Sensors," *CES Transactions on Electrical Machines and Systems*, vol. 5, no. 1, pp. 70–77, Mar. 2021.

[5] G. Liu, Y. F. Liu, and S. Q. Zheng, "Moving-gimbal Effect Suppression for AMB-rotor Systems with Improved Dynamic Response in Control Moment Gyroscopes," *ISA Trans.*, vol. 125, pp. 539–546, Jun. 2022.

[6] Q. Chen, G. Liu, and S. Q. Zheng, "Suppression of Imbalance Vibration for AMBs Controlled Driveline System Using Double-loop Structure," *Journal of Sound and Vibration*, vol. 337, pp. 1–13, Feb. 2015.

[7] W. J. Han, Y. W. Cai, and W. T. Han *et al*., "Review on Active Vibration Control Method of Magnetically Suspended System," *IEEE Access*, vol. 11, pp. 108117–108125, Sept. 2023.

[8] Y. Yubisui, S. Kobayashi, and R. Amano *et al*., "Effects of Nonlinearity of Magnetic Force on Passing Through a Critical Speed of a Rotor with a Superconducting Bearing," *IEEE Transactions on Applied Superconductivity*, vol. 23, no. 3, pp. 5202205–5202205, Jun. 2013.

[9] W. J. Han, Y. W. Cai, and C. M. Yu *et al*., "Harmonic Vibration Suppression of MSCSG based on an Improved Multiple Resonant Controller," *IEEE Sensors Journal*, vol. 25, no. 1, pp. 213–225, Jan. 2025.

[10] J. L. Li, G. Liu, and S. Q. Zheng *et al*., "Micro-jitter Control of Magnetically Suspended Control Moment Gyro Using Adaptive LMS Algorithm," *IEEE/ASME Transactions on Mechatronics*, vol. 27, no. 1, pp. 327–335, Feb. 2022.

[11] J. L. Li, G. Liu, and P. L. Cui *et al*., "An Improved Resonant Controller for AMB-rotor System Subject to Displacement Harmonic Disturbance," *IEEE Transactions on Power Electronics*, vol. 37, no. 5, pp. 5235–5244, May 2022.

[12] R. Herzog, P. Buhler, and C. Gahler *et al*., "Unbalance Compensation Using Generalized Notch Filters in the Multivariable Feedback of Magnetic Bearings," *IEEE Transactions on Control Systems Technology*, vol. 4, no. 5, pp. 580–586, Sept. 1996.

[13] G. Weiss, Q. C. Zhong, and T. C. Green *et al*., "H/sup /spl Infin// Repetitive Control of DC-AC Converters in Microgrids," *IEEE Transactions on Power Electronics*, vol. 19, no. 1, pp. 219–230, Jan. 2004.

[14] S. Jiang, D. Cao, and Y. Li *et al*., "Grid-connected Boost-half-bridge Photovoltaic Microinverter System Using Repetitive Current Control and Maximum Power Point Tracking," *IEEE Transactions on Power Electronics*, vol. 27, no. 11, pp. 4711–4722, Nov. 2012.

[15] M. Zhang, L. Huang, and W. X. Yao *et al*., "Circulating Harmonic Current Elimination of a CPS-PWM-based Modular Multilevel Converter with a Plug-in Repetitive Controller," *IEEE Transactions on Power Electronics*, vol. 29, no. 4, pp. 2083–2097, Apr. 2014.

[16] P. L. Cui, S. Li, and G. Z. Zhao *et al*., "Suppression of Harmonic Current in Active–passive Magnetically Suspended CMG Using Improved Repetitive Controller," *IEEE/ASME Transactions on Mechatronics*, vol. 21, no. 4, pp. 2132–2141, Aug. 2016.

[17] J. L. Li, G. Liu, and P. L. Cui *et al*., "3/2-order Dual-mode Fractional Repetitive Control for Harmonic Vibration Suppression in Magnetically Suspended Rotor," *IEEE Sensors Journal*, vol. 20, no. 24, pp. 14713–14721, Dec. 2020.

[18] K. W. Cai, Z. Q. Deng, and C. Peng *et al*., "Suppression of Harmonic Vibration in Magnetically Suspended Centrifugal Compressor Using Zero-phase Odd-harmonic Repetitive Controller," *IEEE Transactions on Industrial Electronics*, vol. 67, no. 9, pp. 7789–7797, Sept. 2020.

[19] J. L. Li, P. P. Chen, and Y. Pan *et al*., "High-precision Suppression of Harmonic Vibration Force by Repetitive Controller with Triple-loop Structure," *IEEE Transactions on Power Electronics*, vol. 38, no. 9, pp. 10821–10828, Sept. 2023.

[20] C. Peng, J. J. Sun, and C. X. Miao *et al*., "A Novel Cross-feedback Notch Filter for Synchronous Vibration Suppression of an MSFW with Significant Gyroscopic Effects," *IEEE Transactions on Industrial Electronics*, vol. 64, no. 9, pp. 7181–7190, Sept. 2017.

[21] J. J. Pérez-Loya, J. Abrahamsson, and F. Evestedt *et al*., (2015, Oct.). Initial Performance Tests of a Permanent Magnet Thrust Bearing for a Hydropower Synchronous Generator Test-rig. *AI Magazine*. [Online]. Available: https://api.semanticscholar.org/CorpusID:54093046

[22] B. C. Han, Y. L. Chen, and M. X. Li *et al*., "Stable Control of Nutation and Precession for the Radial Four-degree-of-freedom AMB-rotor System Considering Strong Gyroscopic Effects," *IEEE Transactions on Industrial Electronics*, vol. 68, no. 11, pp. 11369–11378, Nov. 2021.

[23] J. C. Fang, S. Q. Zheng, and B. C. Han, "AMB Vibration Control for Structural Resonance of Double-gimbal Control Moment Gyro with High-speed Magnetically Suspended Rotor," *IEEE/ASME Transactions on Mechatronics*, vol. 18, no. 1, pp. 32–43, Feb. 2013.

[24] A. R. Husain, M. N. Ahmad, and A. H. M. Yatim, "Sliding Mode Control with Linear Quadratic Hyperplane Design: an Application to an Active Magnetic Bearing System," in *Proc. of 2007 5th Student Conference on Research and Development*, Selangor, Malaysia, Dec. 2007, pp. 1–6.

[25] M. Ahrens, L. Kucera, and R. Larsonneur, "Performance of a Magnetically Suspended Flywheel Energy Storage Device," *IEEE Transactions on Control Systems Technology*, vol. 4, no. 5, pp. 494–502, Sept. 1996.

[26] M. L. Sun, S. Q. Zheng, and K. Wang *et al*., "Filter Cross-feedback Control for Nutation Mode of Asymmetric Rotors with Gyroscopic Effects," *IEEE/ASME Transactions on Mechatronics*, vol. 25, no. 1, pp. 248–258, Feb. 2020.

[27] E. Kurniawan, A. Az-Zukhruf, and E. B. Pratiwi *et al*., "Notch Filter-based Repetitive Controller for a Class of Linear Systems with Time-varying Periodic Signals," *Journal of Control and Decision*, pp. 1–14, Oct. 2025.

[28] E. Kurniawan, H. G. Harno, and H. Wang *et al*., "Robust Adaptive Repetitive Control for Unknown Linear Systems with Odd-harmonic Periodic Disturbances," *Sci. China Inf. Sci.*, vol. 65, pp. 222202, Nov. 2022.

[29] A. M. Diab, S. Bozhko, and M. Galea *et al*., "Stable and Robust Design of Active Disturbance-rejection Current Controller for Permanent Magnet Machines in Transportation Systems," *IEEE Transactions on Transportation Electrification*, vol. 6, no. 4, pp. 1421–1433, Dec. 2020.

[30] Y. F. Liu, G. Liu, and S. Q. Zheng *et al*., "A Modified Active Disturbance Rejection Control Strategy based on Cascade Structure with Enhanced robustness," *ISA Transactions*, vol. 129, part B, pp. 525–534, Oct. 2022.

[31] C. W. Jin, Z. D. Hong, and G. Cui *et al*., "Adaptive Smith Predictive Active Disturbance Rejection Control of Magnetic Suspended Rotor System Considering Time Delay," *IEEE Trans. on Ind. Electron.*, vol. 72, no. 9, pp. 9645–9655, Sept. 2025.

[32] C. Wang, S. Q. Zheng, and J. J. Xie, "Decoupling Control for High-speed Magnetically Suspended Rotor Systems Using Linear Active Disturbance Rejection Method," in *Proc. of 2018 37th Chinese Control Conference*, Wuhan, China, Jul. 2018, pp. 3885–3892.

[33] M. H. Tian, B. Wang, and Y. Yu *et al*., "Discrete-time Repetitive Control-based ADRC for Current Loop Disturbances Suppression of PMSM Drives," *IEEE Transactions on Industrial Informatics*, vol. 18, no. 5, pp. 3138–3149, May 2022.

[34] Q. S. Zhao, Q. F. Wang, and H. W. Zhang *et al*., "A Novel RC-ESO-ADRC for Harmonics Suppression and Robustness Improvement of

Grid-tied Inverters in a Weak and Distorted Grid," *IEEE Transactions on Power Electronics*, vol. 40, no. 9, pp. 12581–12593, Sept. 2025.

[35] Q. Zheng, Z. Z. Chen, and Z. Q. Gao, "A Practical Approach to Disturbance Decoupling Control," *Control Engineering Practice*, vol. 17, no. 9, pp. 1016–1025, Sept. 2009.

[36] C. F. Fu, and W. Tan, "Tuning of Linear ADRC with Known Plant Information," *ISA Trans.*, vol. 65, pp. 384–393, Nov. 2016.

Yuxiang Zhu received the B.S. degree in electrical engineering from Tsinghua University, Beijing, China, in 2023. Yuxiang Zhu is currently working toward the Ph.D degree in the Institute of Electrical Engineering, Chinese Academy of Sciences, and the University of Chinese Academy of Sciences, Beijing, China. His research interests include active magnetic bearings and transformer design.

Fanqiang Gao (Member, IEEE) was born in Hubei, China, in 1984. He received the B.Eng. degree in automation control from the Huazhong University of Science and Technology, Wuhan, China, in 2006 and the Ph.D. degree in power electronics and power drives from the Institute of Electrical Engineering, Chinese Academy of Sciences, Beijing, China, in 2012.

He joined the Institute of Electrical Engineering, Chinese Academy of Sciences, in 2012, where he is currently an Associate Professor. His research interests include the analysis and control of power electronic converters in high power fields.

Kaiyu Shan was born in Liaoning, China, in 2000. He received the B.S. degree in electrical engineering from Northeast Electric Power University, Jilin, China, in 2023. He is currently working towards his Ph.D. degree in electrical engineering with the Institute of Electrical Engineering, Chinese Academy of Sciences, and the University of Chinese Academy of Sciences, Beijing, China. His research interest includes magnetic bearing control and permanent magnet synchronous motor control.

Zixin Li (Senior Member, IEEE) was born in Hebei, China, in 1981. He received the B.Eng. degree in industry automation from the North China University of Technology, Beijing, China, in 2005, and the Ph.D. degree in Power Electronics and Power Drives from the Institute of Electrical Engineering, Chinese Academy of Sciences, Beijing, China, in 2010.

Since 2010, he has been with the Institute of Electrical Engineering, Chinese Academy of Sciences, where he is currently a Professor and Deputy Director. He has authored or coauthored more than one hundred academic papers and holds more than twenty invention patents in China. His research interests include power electronics and electromagnetic drive technologies and their applications in power grids, transportation, energy, and other fields.

Dr. Li is currently serving, or has previously served, as an Associate Editor for IEEE Transactions on Power Electronics, IET High Voltage, Journal of Power Electronics, and Chinese Journal of Electrical Engineering. He was the recipient of the IEEE Power Electronics Society Richard M. Bass Outstanding Young Power Electronics Engineer Award of 2015 for his contributions to multilevel and HVDC converters. He was elected as a Fellow of the Institution of Engineering and Technology (IET) in 2019.

Yaohua Li (Member, IEEE) was born in Henan, China, in 1966. He received the Ph.D. degree in power electronics and power drives from Tsinghua University, Beijing, China, in 1994. From 1995 to 1997, he was a Post-Doctoral Research Fellow with the Institute of Electrical Machines, Technical University of Berlin, Berlin, Germany. In 1997, he joined the Institute of Electrical Engineering, Chinese Academy of Sciences, Beijing, where he is currently working as a Professor and the Director. His current research interests include the analysis and control of electrical machines and power electronics.